Controlling collective properties of supported metal nanoparticles: towards stable catalysts

Gonzalo Prieto[1], Jovana Zečević[1], Heiner Friedrich[2], Krijn P. de Jong[1,*] and Petra E. de Jongh[1,*]

[1] Inorganic Chemistry and Catalysis, Debye Institute for Nanomaterials Science, Utrecht University, The Netherlands

[2] Laboratory of Materials and Interface Chemistry, Eindhoven University of Technology, Eindhoven, The Netherlands

[*]Corresponding authors: k.p.deJong@uu.nl and p.e.deJongh@uu.nl

Supported metal nanoparticles play a pivotal role in areas such as nanoelectronics, energy storage/conversion[1] and as catalysts for the sustainable production of fuels and chemicals[2,3,4]. However, the tendency of nanoparticles to grow into larger crystallites is an impediment for stable performance[5,6]. Exemplary, loss of active surface area by metal particle growth is a major cause of deactivation for supported catalysts[7]. In specific cases particle growth might be mitigated by tuning the properties of *individual* nanoparticles, such as size[8], composition[9] and interaction with the support[10]. Here we present an alternative strategy based on control over *collective* properties, revealing the dramatic impact of the 3D nanospatial distribution of metal particles on catalyst stability. We employ silica-supported copper nanoparticles as catalysts for methanol synthesis as a showcase. Achieving near-maximum interparticle spacings, as accessed quantitatively by electron tomography, slows down deactivation up to an order of magnitude compared to a catalyst with non-uniform nanoparticle distribution, or a reference Cu/ZnO/Al_2O_3 catalyst. Our approach paves the way towards rational design of practically relevant catalysts and other nanomaterials with enhanced stability and functionality, for applications such as in catalysis, sensors, gas storage, batteries, and solar fuels production.

Metal nanoparticle growth can proceed via migration and coalescence of particles (sintering) or via transport of monoatomic or molecular species between individual particles (Ostwald ripening)[7]. Strategies to mitigate particle growth comprise alloying with a higher-melting point metal[9] and increasing the metal-support interaction energy by using specific oxides as carrier[10]. However, these approaches are not generally applicable since they restrict the catalyst chemical composition and therefore function. Recently, the encapsulation of individual colloidal nanoparticles in porous inorganic shells has received much attention[11,12]. Albeit conceptually elegant, bottom-up approaches at the *single-nanoparticle level* face challenges for large scale production and usage. We present an alternative approach, using nanoparticle assembly tools to tune the stability-relevant *collective* properties of supported metal particles, i.e. their spatial distribution at the nanoscale.

Metal nanoparticles dispersed on a porous carrier are widely used as solid catalysts[13]. Irregular spatial distributions and ultra-short interparticle distances are quite common for technical catalysts. For instance,

clustering of metal nanoparticles in high-density assemblies is known to occur for Ni-Mo/Al_2O_3 and Co-Pt/Al_2O_3 catalysts industrially employed in processes such as the sulphur-removal from hydrocarbon feedstocks and the Fischer-Tropsch synthesis of fuels from synthesis gas, respectively[13,14]. Also, commercial methanol synthesis catalysts typically consist of Cu particles (ca. 5-10 nm) only spaced by smaller ZnO crystallites[15]. Nanoparticles spatial distributions might have large significance for catalyst stability, given that metal particle growth is a relevant deactivation mechanism for commercial catalysts. Though on a micrometer-scale metal distributions can be controlled to some extent (for instance "egg-shell" or "egg-yolk" distributions), the 3D spatial distribution of metal particles on a nanometers scale is until now typically an uncontrollable outcome of the preparation process. In contrast, our work shows control over size and location of active metal species while employing industrially relevant preparation tools, in this case impregnation of porous carriers with inexpensive metal precursors such as nitrates[16,17,18].

Quantitative information on the 3D nanospatial distribution of the metal particles is indispensable if we want to understand supported nanoparticles stability, and progress from 2D flat model substrates towards more realistic 3D support morphologies. This information is provided by electron tomography (ET), which has emerged as a major tool in material science[19,20,21]. ET allows derivation of metal particle size distributions and nanospatial locations. In this work we additionally employ pore-specific analysis, which relates particle locations to the local support pore morphology. We combine these tools to demonstrate exceptional stability by control over the nanospatial distribution of supported metal particles, using Cu-Zn/SiO_2 catalysts for methanol synthesis as a case in point.

The industrial production of methanol from synthesis gas ($CO/CO_2/H_2$) amounts worldwide to more than $35 \cdot 10^6$ t/year and uses Cu/ZnO/Al_2O_3 as a catalyst. Growth of the Cu crystallites is the main deactivation pathway under standard plant conditions. In this study we employ as support material ordered mesoporous silica (SBA-15[22]) rather than industrial Al_2O_3 to facilitate quantitative image analysis. Also samples based on industrial SiO_2-gel supports with 3D interconnected pore networks were investigated to validate the wider significance of our results. The CuZn/SiO_2 catalysts were prepared by impregnation using an aqueous solution of metal nitrates. Building on recent mechanistic insight[17], for the first time we succeeded in preparing exclusively <6 nm Cu nanoparticles at relatively high metal loadings. In particular, effective water removal at low temperatures was essential to avoid the large metal agglomerates and bimodal size distributions previously observed[17] (see Supplementary Methods). The dried impregnate was heated to 723 K (referred to as calcination hereafter) under either N_2 or 2%NO/N_2 flow. Samples are labelled as CuZn/x(y), where x=S (SBA-15) or Sgel (SiO_2-gel) and y= N_2 or NO according to the calcination atmosphere. A Cu/ZnO/Al_2O_3 reference catalyst was prepared by co-precipitation route representative for commercial catalysts[23]. This reference catalyst showed similar copper-weight-based initial catalytic activity, validating our approach to use an ordered silica model support.

Table 1 gives an overview of the structural properties of the catalysts. Mean Cu^0 crystallite sizes were 2.4-9.7 nm after H_2-reduction, whereas crystalline Zn compounds were not detected. Zn species are essential in promoting the catalytic Cu particles to achieve optimum methanol productivity[24]. Close contact between Cu and

Zn (oxide) is prerequisite for this synergism[25]. X-ray absorption spectroscopy showed the high dispersion of Zn species on the surface of the silica support (Supplementary Fig. S1). Energy-dispersive X-ray spectroscopy (EDX) evidenced that the required intimacy between Zn and Cu on the nanoscale is achieved regardless of the calcination procedure (Supplementary Fig. S2). Hence, hereafter the discussion will focus on the Cu particles. The CuZn/SBA-15 catalysts exposed similar Cu^0 surface areas (104-118 m^2/g_{Cu}), approximately double that of the $Cu/ZnO/Al_2O_3$ reference sample, albeit at four times lower Cu content. Thus, bulk characterization techniques point to little difference between the SiO_2-supported catalysts obtained by calcination in either N_2 or $2\%NO/N_2$ flow. However, these characterization methods lack spatial resolution. Scanning-transmission electron microscopy (STEM) gave a first indication of different spatial distribution of the active Cu phase (Supplementary Fig. S2). Nonetheless, conventional (S)TEM implies averaging information over the entire thickness of the support particle, e.g. here >20 superimposed mesopores.

Table 1 | Structural and catalytic properties of the studied catalysts.

Catalyst	$S_{B.E.T}$ [a] [$m^2\ g_{SiO2}^{-1}$]	PV_{meso} [b] [$cm^3\ g_{SiO2}^{-1}$]	Cu [c] [wt-%]	S_{Cu} [d] [$m^2\ g_{Cu}^{-1}$]	$d(Cu)_{XRD}$ [e] [nm]	MeOH yield [f] [mol $g_{Cu}^{-1}\ h^{-1}$]	MeOH select. [g] [C-%]	$k_{D,2}$ [h] [$10^{-3}\ h^{-1}$]
SBA-15	775	0.79	---	---	---	---	---	---
CuZn/S(NO)	657	0.68	12.2	118	3.5	0.11	98.3	4.4
CuZn/S(N_2)	623	0.71	11.5	104	2.4	0.09	97.8	0.9
SiO_2-gel	354	1.00	---	---	---	---	---	---
CuZn/Sgel(NO)	318	0.81	11.8	---	5.9	0.10	98.3	20.3
CuZn/Sgel(N_2)	286	0.78	10.7	---	9.7	0.11	98.5	5.9
$Cu/ZnO/Al_2O_3$	---	---	51.4	59	5.1	0.13	99.6	8.9

[a] Specific B.E.T. surface area. [b] Mesopore volume. [c] Copper loading. [d] Specific Cu surface area for the as-reduced catalyst, as determined by N_2O reactive frontal chromatography. [e] Mean Cu^0 crystallite size for the as-reduced catalyst, as determined by X-ray diffraction-monitored in situ H_2-reduction. [f] Initial methanol yield; reaction conditions: T=533 K, P=40 bar, synthesis gas feedstock $Ar:CO_2:CO:H_2=10:7:23:60$ (vol), initial $(CO+CO_2)$ conversion of 15-20%. [g] Steady (time-on-stream>100 h) selectivity to methanol (dimethylether is the only significant side-product) [h] Second-order deactivation rate constant obtained after fitting the deactivation profile with a second-order deactivation law: $da/dt=-k_{D,2}\cdot a^2$, where a denotes the normalized methanol productivity.

We used ET combined with image analysis to provide precise 3D information on the size, shape and location of the individual Cu nanoparticles. The size and position of all particles in a tomogram was obtained by automatic segmentation (Supplementary Information, section 5.1), but more importantly also pore-specific manual segmentation was applied as illustrated in Figure 1. This analysis allowed acquisition of the in-pore surface-to-surface interparticle distances, which are presumably crucial for growth, irrespective of whether caused by sintering or by Ostwald ripening.

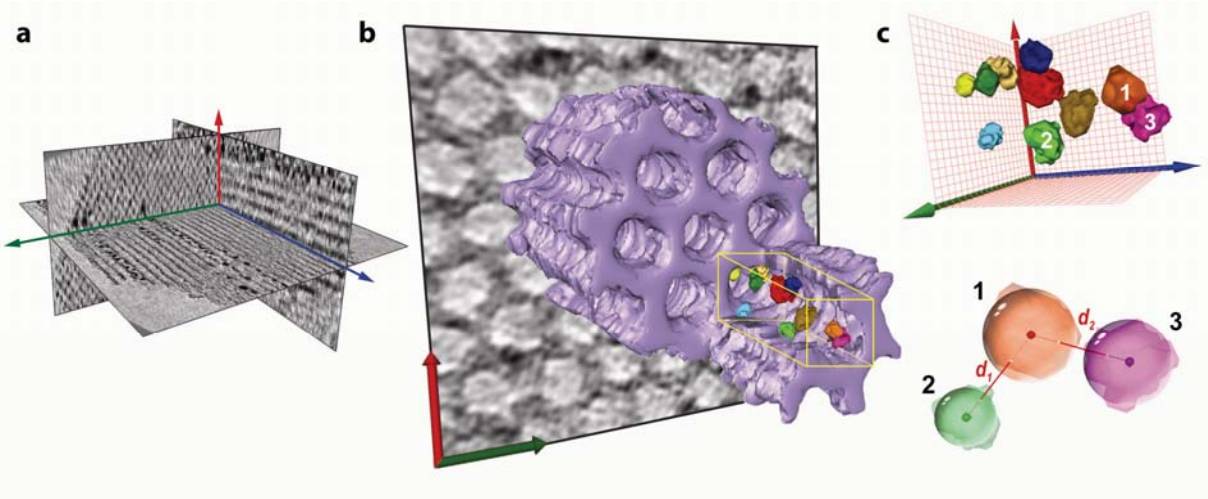

Figure 1 | How statistically relevant, pore-specific information on the size and 3D nanospatial distribution of metal particles is derived from electron tomograms. a, Orthogonal cross-sections through the 3D reconstructed tomogram of a representative particle of a nanostructured catalyst. The SiO_2 pore walls are grey and the metal nanoparticles appear as black spots. **b,** 3D-rendered volume obtained by image segmentation showing the hexagonal arrangement of the catalyst mesopores as well as details on the internal corrugation of the silica pore walls. One of the reconstructed mesopores has been partially sectioned to visualize the individually-segmented Cu nanoparticles. **c,** 3D-view of the isolated Cu nanoparticles extracted from the volume indicated with a yellow frame in panel b. The approximation of the metal particles by volume-equivalent spheres centred at their center of gravity and the derivation of surface-to-surface interparticle distances is schematically depicted. For validation of the statistical relevance of our analysis results see sections 5.1 and 5.2 in the Supplementary Information.

[Figure 1: 17 x 7 cm (double column)]

Figure 2 summarizes the electron tomography results for the as-prepared CuZn/SBA-15 catalysts after H_2-reduction, giving cross-sections through the reconstructed 3D volumes (a-b, e-f), Cu particle size (c,g) and neighbor-distance distributions (d,h). Full electron tomograms are given as Supplementary Videos 1 and 2. For CuZn/S(NO) (panels a-d) a fraction of the pores contained high metal loadings, while other pores hosted virtually no metal particles. A surface-averaged Cu particle size of 5.7±2.0 nm was derived from the corresponding size histogram. The uneven distribution of the catalytic particles in the pore system resulted in distance distributions centred at 2.7 and 7.9 nm for the nearest and second-nearest neighbors, respectively. Such irregular spatial distribution and short interparticle distances are quite common for technical catalysts.

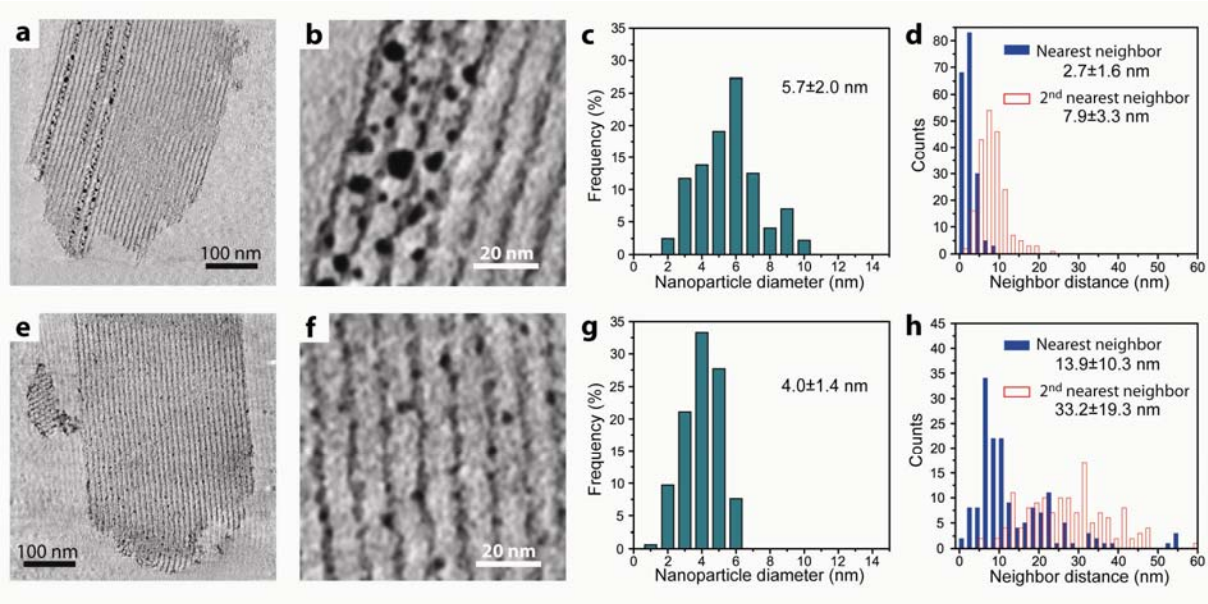

Figure 2 | Quantitative electron tomography results for CuZn/SBA-15 catalysts after H_2-reduction. The figure includes cross-sections through the 3D-reconstructed tomograms (**a-b** and **e-f**), surface-weighted Cu nanoparticle size histograms (**c,g**) and surface-to-surface nearest-neighbors distance histograms (**d,h**) for the Cu particles in the CuZn/SBA-15 catalysts calcined under a flow of 2%NO/N_2 (**a-d**) or a flow of N_2 (**e-h**), and subsequently reduced in 20%H_2/N_2. The values for the average and standard deviation are included in the histograms. Cu particles hosted in the same silica pore were considered to generate the interparticle distance histograms.

[Figure 2: 17 x 8.5 cm (double column)]

Recent insight into *ex*-nitrate catalyst synthesis suggested strategies to control the spatial distribution of the active Cu species[17]. Starting point was the distribution of the metal nitrate precursors within the support porosity after impregnation and drying (Supplementary Fig. S3). Calcination in the presence of NO promoted hydrolysis forming $Cu_2(OH)_3NO_3$ which has a low surface mobility. Minimized metal redistribution led to the typical patchwise distribution discussed above. However, by efficient vacuum-drying at room temperature followed by calcination in N_2 flow we prevented premature hydrolysis, enabling now full exploitation of Cu redispersion via a mobile anhydrous $Cu(NO_3)_2$ intermediate over the SiO_2 surface. Despite the similarities in average structural properties accessed by bulk characterization techniques, ET revealed a large impact of the calcination procedure on the nanospatial distribution of the Cu nanoparticles.

The N_2-calcined catalyst (panels e-h) comprised Cu particles with a narrow size distribution (4.0±1.4 nm) which, in marked contrast to CuZn/S(NO), were evenly distributed throughout the entire pore system. This homogeneous distribution is further illustrated by the broad neighbor-distance distributions (Fig. 2h). The average distances of 13.9 and 33.2 nm to the nearest and second-nearest neighbors, respectively, were 4-5 fold higher than for CuZn/S(NO). Remarkably, they were very close to the theoretical maximum neighbor distances (14.9 and 31.1 nm) for 4 nm-sized Cu particles at the given Cu loading. Hence, CuZn/S(N_2) featured a distribution which seems ideal for a growth-resistant catalyst, *i.e.* equally sized (minimum driving force for ripening) and maximally spaced metal nanoparticles. We focused on catalysts supported on SBA-15 silica as their well defined pore structure facilitates visualization and quantitative analysis of the results, although correspondingly, Cu nanoparticles

gathered in 3D high-density domains or uniformly distributed were found by ET in as-reduced $CuZn/SiO_2$-gel catalysts calcined in NO/N_2 or N_2, respectively (Supplementary Fig. S4).

Excellent studies on the nanoparticle growth mechanisms and rates have been reported using *in situ* TEM, applying very low pressures (typically a few mbars) and elevated temperatures[26,27,28]. However, deactivation rates and pathways are known to depend strongly on the gas atmosphere and pressure. We decided to test the catalytic stability under realistic conditions for methanol synthesis. A reaction temperature of 533 K, among the highest of industrially applied temperatures, was employed to study deactivation within laboratory time-scales. The $CuZn/SiO_2$ catalysts displayed remarkably high initial copper-normalized methanol production activity, less than 30% lower than the $Cu/ZnO/Al_2O_3$ reference catalyst (Table 1). However, striking differences in stability were observed as illustrated in Fig. 3. A fast activity decay was observed for the reference $Cu/ZnO/Al_2O_3$ catalyst as well as NO-calcined $CuZn/SiO_2$ catalysts displaying high-density particle domains. Employing a support with 1D instead of 3D interconnected porosity reduced the activity loss, as illustrated by comparing CuZn/Sgel(NO) and CuZn/S(NO). Most remarkably, the activity decline was radically slower if for a given support the nanospatial distribution of the metal particles was optimized to achieve near-maximum interparticle spacings, with $CuZn/S(N_2)$ retaining even >82% of the initial activity after 240 hours. Structural damage to the silica support did not contribute to the decay, as even the SBA-15 supported samples (Supplementary Table S1) showed no significant pore volume loss. Generally, small nanoparticles are more prone to grow than larger ones[8]. However in the present investigation the sample with the smallest particles, *i.e.* $CuZn/S(N_2)$ shows the highest stability. Hence its superior stability can be ascribed to the specific spatial distribution of the active nanoparticles. Deactivation rate constants can be consistently compared using second order deactivation (Table 1 and Supplementary Figure S5). A roughly four-fold decrease in the second order deactivation rate constant was achieved for samples with uniform spatial distribution of the metal nanoparticles with respect to those containing high-density particle domains, and up to one order in magnitude with respect to the reference $Cu/ZnO/Al_2O_3$ catalyst.

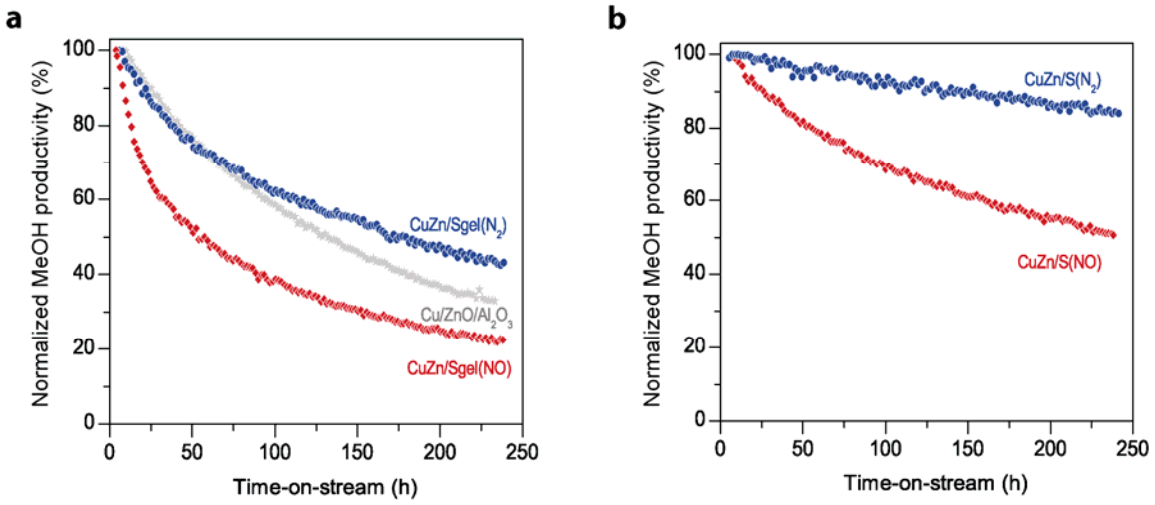

Figure 3 | Catalytic testing of $CuZn/SiO_2$ and $Cu/ZnO/Al_2O_3$ catalysts. The figure plots the evolution of the normalized methanol productivity versus the time-on-stream for $CuZn/SiO_2$-gel (a) and CuZn/SBA-15 (b) catalysts calcined under a flow of $2\%NO/N_2$ or a flow of N_2, as well as for a $Cu/ZnO/Al_2O_3$ catalyst synthesised according to conventional co-precipitation procedure typical of industrial catalysts (included in panel a). Reaction conditions: synthesis gas feedstock $7\%CO_2$:23%CO:$60\%H_2$:10%Ar (internal standard), T=533 K, P=40 bar, gas hourly space velocity (GHSV) of 2-3 $L{\cdot}g^{-1}{\cdot}h^{-1}$, initial conversion ($CO+CO_2$) =(15-20%).

[Figure 3: 8.8 x 7 cm (single column)]

Electron tomography was also employed to analyse the CuZn/SBA-15 catalysts after 10 days of catalysis (Fig. 4). Full electron tomograms are given as Supplementary Videos 3 and 4. Due to prolonged exposure to catalysis, the surface-averaged particle sizes had overall increased with 30-45%. Particle size histograms translate into a decrease in Cu surface area of 23.5% and 33.1% for $CuZn/S(N_2)$ and CuZn/S(NO), respectively, in reasonable agreement with the decrease in catalytic activity. Deviations might originate from a slight particle size dependence of the specific activity, and/or a change in the effectiveness of Zn promoter species upon Cu particle growth. TEM revealed severe Cu particle growth for the reference $Cu/ZnO/Al_2O_3$ during catalysis (Supplementary Fig. S6).

There has been extensive debate about which particle growth mechanism is most relevant under industrial conditions. *In situ* microscopic observations, limited to sub-atmospheric pressures, suggest surface diffusion-mediated Ostwald ripening rather than migration-coalescence as a major pathway, particularly in the presence of oxidant species such as O_2, CO_2 or H_2O[26,28,29]. Higher CO_2 and H_2O partial pressures are found under realistic methanol synthesis conditions as those applied in this study. Under our experimental conditions, the notorious impact of interparticle distance on catalyst deactivation additionally points to kinetic relevance of diffusion phenomena.

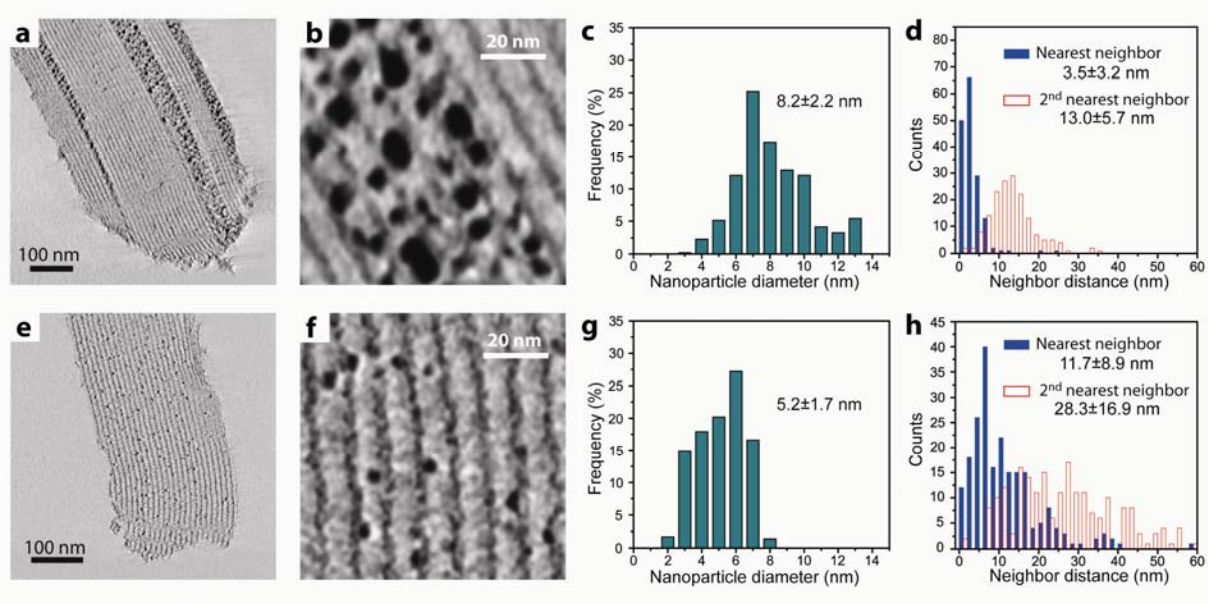

Figure 4 | Quantitative electron tomography results for CuZn/SBA-15 catalysts after exposure to reaction conditions. The figure includes cross-sections through the 3D-reconstructed tomograms (**a-b** and **e-f**), surface-weighted Cu nanoparticle size histograms (**c,g**) and the surface-to-surface nearest-neighbors distance histograms (**d,h**) for the Cu particles in the CuZn/SBA-15 catalysts calcined under a flow of 2%NO/N_2 (**a-d**) or a flow of N_2 (**e-h**), after exposure to methanol synthesis conditions for 240 hours. The values for the average and standard deviation are included in the histograms. Cu particles hosted in the same silica pore were considered to generate the interparticle distance histograms.

[Figure 4: 17 x 8.5 cm (double column)]

Classically, mean-field models[7], based on sheer particle size effects, are used to describe metal ripening. However, these failed to describe our results (see Supplementary Information). We are not aware of any previous literature for ripening in 3D catalysts described using models that do take the spatial location of the individual particles into account. Owing to the lack of accurate information on metal spatial distribution in 3D systems so far, results are only available for flat model systems[27,30]. As a first step, we used a diffusion-controlled ripening mechanism to describe the quantitative results from image analysis (see Supplementary Information). This kinetic model offered a reasonable description of the results for near-maximum interparticle spacings, i.e. CuZn/S(N_2), provided we assume strong local correlations, i.e. only nearest and second-nearest neighbors in the same SiO_2 pore contribute significantly to growth/decay rates of other particles. This further exemplifies the significance of the spatial distribution for particle growth. However, for the catalyst with a clustered distribution of the Cu nanoparticles, diffusion-limited ripening could not fully explain the particle growth observed. Apparently, for short interparticle distances an alternative pathway, likely particle migration-coalescence, gains importance. Supporting this hypothesis, ET revealed a significant increment in interparticle spacing (30% and 65% on average for nearest and second-nearest neighbors, respectively) upon exposure of CuZn/S(NO) to catalysis, while several tomographic cross-sections (e.g. in Fig. 4b) showed dumbbell-shaped Cu particles as intermediates in particle coalescence. Dumbbell shaped particles are expected to have a short lifetime at these elevated temperatures. The fact that we nevertheless observe them suggests these are rather frequently occurring events, while probably corrugation of the pore walls (Fig. 1) adds to stabilisation of the shape. Our analysis highlights the importance of considering the 3D

spatial location of metal nanoparticles to describe metal particle growth in realistic supported catalysts and provides a starting point to develop more advanced particle growth models.

In summary, advanced control over catalyst design based on recent fundamental progress in the assembly of supported catalysts was coupled to unprecedented quantitative information on the 3D nanospatial distribution of supported metal nanoparticles provided by electron tomography. This unique combination allowed comparing, under industrially relevant conditions, the stability of Cu-based methanol synthesis catalysts with similar overall properties, but differing vastly on the distribution of active particles at the nanoscale. We demonstrate the tremendous importance of not only considering individual properties of the catalytic nanoparticles, such as the particle size, but also collective properties such as their relative spatial location. Our study highlights how to progress from detailed in-situ TEM and 2D model support studies towards describing particle growth in realistic 3D supported systems under industrially relevant conditions. At least as important, our work provides a new approach towards designing and assembling catalysts and related functional nanostructured materials with high durability.

Methods summary

$CuZn/SiO_2$ catalysts were synthesised by incipient wetness impregnation of the silica supports with a 4M aqueous solution of copper and zinc nitrates (atomic ratio Cu/Zn=65/35). The impregnates were dried for 12 h at RT under dynamic vacuum and subsequently calcined at 723 K for 1 hour under a flow of either pure N_2 or 2%NO/N_2(v/v) at GHSV=$1.0 \cdot 10^4$ h^{-1}. Methanol synthesis catalytic tests were performed at 40 bar and 533 K in a stainless steel reactor using a feedstock composition of Ar:CO_2:CO:H_2=10:7:23:60 (vol.). Prior to catalysis, the catalysts were reduced in situ at 523 K for 150 min. under a flow of 20%H_2/Ar (vol.). Electron tomography was performed on a Tecnai 20 (FEI) microscope operated at 200 kV. TEM images were collected over a tilt range of at least ±70º with tilt increments of 1º or 2º, at a nominal magnification of 25k-50k. The 3D reconstructions of the aligned tilt series were obtained using the simultaneous iterative reconstruction technique (SIRT). Further details on the experimental methods can be found in the Supplementary Information.

Acknowledgements

Hans Meeldijk, Marjan Versluijs, Rien van Zwienen and Ad van der Eerden (Utrecht University) are acknowledged for HAADF-STEM/EDX analysis, in situ XRD measurements, assistance with the high-pressure catalytic setup and discussions on the XAS data, respectively. Dr. M. Watson, Dr. L. van de Water and C. Ranson (Johnson Matthey Catalysts) are thanked for the N_2O RFC measurements. The ET study was carried out in the 3D Electron Microscopy group of Utrecht University headed by Dr. Willie Geerts and Dr. J. Andries Post. Beamline C at Hasylab (Hamburg) is acknowledged for the beamtime allocated (project I-20110876 EC). This material is largely based upon work supported as part of the Center for Atomic-Level Catalyst Design, an Energy Frontier Research Center funded by the U.S. Department of Energy, Office of Science, Office of Basic Energy Sciences under Award Number DE-SC0001058; additional support from NRSCC and NWO is acknowledged.

Author Contributions

P.E.dJ and K.P.dJ conceived and designed the research. G.P. synthesized the catalysts and ran the catalytic tests. J.Z. recorded the TEM tilt-series. J.Z. and G.P. reconstructed the electron tomograms and carried out image segmentation with guidance of H.F. G.P. designed the routines and performed the particle growth simulations. The manuscript was primarily written by G.P and P.E.dJ. All authors contributed to discussions and manuscript review.

Author Information

The authors declare no competing financial interests. Supplementary Information accompanies this paper on www. nature.com/naturematerials. Reprints and permissions information is available online at www.nature.com/reprints. Correspondence and requests for materials should be addressed to K.P. de Jong (k.p.deJong@uu.nl) and P.E. de Jongh (p.e.deJongh@uu.nl).

References

[1] Aricò, A. S., Bruce, P., Scrosati, B., Tarascon, J. M., van Schalkwijk, W. Nanostructured materials for advanced energy conversion and storage devices. *Nature Mater*. **4,** 366 – 377 (2005).

[2] Román-Leshkov, Y., Barret, C. J., Liu, Z. Y., Dumesic, J. A. Production of dimethylfuran for liquid fuels from biomass-derived carbohydrates. *Nature* **447,** 982-985 (2007).

[3] Kesavan, L., Tiruvalam, R., Rahim, M. H. A., Bin Saiman, M. I., Enache, D. I., Jenkins, R. L., Dimitratos, N., Lopez-Sanchez, J. A., Taylor, S. H., Knight, D. W., Kiely, C. J., Hutchings, G. J. Solvent-free oxidation of primary carbon-hydrogen bonds in toluene using Au-Pd alloy nanoparticles. *Science* **14,** 195-199 (2011).

[4] Torres Galvis, H. M., Bitter, J. H., Khare, C. B., Ruitenbeek, M., Dugulan, A. I., de Jong, K. P., Supported iron nanoparticles as catalysts for sustainable production of lower olefins. *Science* **17,** 835-838 (2012).

[5] Newton, M. A., Belver-Coldeira, C., Martínez-Arias, A., Fernández-García, M. Dynamic in situ observation of rapid size and shape change of supported Pd nanoparticles during CO/NO cycling. *Nature Mater.* **6,** 528 – 532 (2007).

[6] Xin, H. L., Mundy, J. A., Liu, Z., Cabezas, R., Hovden, R., Kourkoutis, L. F., Zhang, J., Subramanian, N. P., Makharia, R., Wagner, F. T., Muller, D. A. Atomic-resolution spectroscopic imaging of ensembles of nanocatalyst particles across the life of a fuel cell. *Nano Lett.* **12,** 490-497 (2012).

[7] Wynblatt, P., Gjostein, N. A. Supported metal crystallites. *Prog. Solid State Chem.* **9,** 21-58 (1975).

[8] Campbell, C. T., Parker, S. C., Starr, D. E. The effect of size-dependent nanoparticle energetics on catalyst sintering. *Science* **298,** 811-814 (2002).

[9] Cao, A., Veser, G. Exceptional high-temperature stability through distillation-like self-stabilization in bimetallic nanoparticles. *Nature Mater.* **9,** 75-81 (2010).

[10] Farmer, J. A., Campbell, C. T. Ceria maintains smaller metal catalyst particles by strong metal-support bonding. *Science* **329,** 933-936 (2010).

[11] Arnal, P. M., Comotti, M., Schüth, F. High-temperature-stable catalysts by hollow sphere encapsulation. *Angew. Chem.* **118,** 8404-8407 (2006); *Angew. Chem. Int. Ed.* **45,** 8224-8227 (2006).

[12] Joo, S. H. Park, J.Y., Tsung, C.K., Yamada, Y., Yang, P., Somorjai, G.A. Thermally stable Pt/mesoporous silica core-shell nanocatalysts for high temperature reactions. *Nature Mater.* **8,** 126-131 (2009).

[13] De Jong, K. P. (Ed.). *Synthesis of Solid Catalysts*. Wiley-VCH (Weinheim, 2009).

[14] Saib, A. M., Moodley, D.J., Ciobîcă, I.M., Hauman, M.M., Sigwebela, B.H., Weststrate, C.J., Niemantsverdriet, J.W., van de Loosdrecht, J. Fundamental understanding of deactivation and regeneration of cobalt Fischer–Tropsch synthesis catalysts. *Catal. Today* **154,** 271-282 (2010).

[15] Ressler, T., Kniep, B.L., Kasatkin, I., Schlögl, R. The microstructure of copper zinc oxide catalysts: bridging the materials gap. *Angew. Chem.* **117,** 4782–4785 (2005) ; *Angew. Chem. Int. Ed.* **44,** 4704 –4707 (2005).

[16] Sietsma, J. R. A., Meeldijk, J.D., den Breejen, J.P., Versluijs-Helder, M., van Dillen, A.J., de Jongh, P.E., de Jong, K.P. The preparation of supported NiO and Co_3O_4 nanoparticles by the nitric oxide controlled thermal decomposition of nitrates. *Angew. Chem.* **119,** 4631–4633 (2007); *Angew. Chem. Int. Ed.* **46,** 4547–4549 (2007).

[17] Friedrich, H., Sietsma, J. R. A., de Jongh, P. E., Verkleij, A. J., de Jong, K. P. Measuring location, size, distribution and loading of NiO crystallites in individual SBA-15 pores by electron tomography. *J. Am. Chem. Soc.* **129,** 10249-10254 (2007).

[18] Munnik, P., Wolters, M., Gabrielsson, A., Pollington, S. D., Headdock, G., Bitter, J. H., de Jongh, P. E., de Jong, K. P. Copper nitrate redispersion to arrive at highly active silica-supported copper catalysts. *J. Phys. Chem. C* **115,** 14698–14706 (2011).

[19] Midgley, P., Dunin-Borkowski, R. E. Electron tomography and holography in materials science. *Nature Mater.* **8,** 271-280 (2009).

[20] Friedrich, H. , de Jongh, P. E., Verkleij, A. J., de Jong, K. P. Electron tomography for heterogeneous catalysts and related nanostructured materials. *Chem. Rev.* **109,** 1613-1629 (2009).

[21] Kiely, C. *Nature Mater*. **9,** 296-297 (2010).

[22] Zhao, D., Feng, J., Huo, Q., Melosh, N., Fredrickson, G.H., Chmelka, B.F., Stucky, G.D. Triblock copolymer syntheses of mesoporous silica with periodic 50 to 300 angstrom pores. *Science* **23,** 548-552 (1998).

[23] Baltes, C., Vukojević, S., Schüth, F. Correlations between synthesis, precursor, and catalyst structure and activity of a large set of $CuO/ZnO/Al_2O_3$ catalysts for methanol synthesis. *J. Catal.* **258,** 334-344 (2008**).**

[24] Kasatkin, I., Kurr, P., Kniep, B., Trunschke, A., Schlögl, R. Role of lattice strain and defects in copper particles on the activity of $Cu/ZnO/Al_2O_3$ catalysts for methanol synthesis. *Angew. Chem.* **38,** 7465–7468 (2007) ; *Angew. Chem. Int. Ed.* **46,** 7324-7327 (2007).

[25] Becker, R., Parala, H., Hipler, F., Tkachenko, O.P., Klementiev, K.V., Grünert, W., Wilmer, H., Hinrichsen, O., Muhler, M., Birkner, A., Wöll, C., Schäfer, S., Fischer R.A. MOCVD-loading of mesoporous siliceous matrices with Cu/ZnO: supported catalysts for methanol synthesis. *Angew. Chem.* **116,** 2899–2903 (2004) ; *Angew. Chem. Int. Ed.* **43,** 2839–2842 (2004).

[26] Simonsen, S. B., Chorkendorff, I., Dahl, S., Skoglundh, M., Sehested, J., Helveg, S., Direct observation of oxygen-induced platinum nanoparticle ripening studied by in situ TEM. *J. Am. Chem. Soc*. **132,** 7968-7975 (2010).

[27] Simonsen, S. B., Chorkendorff, I., Dahl, S., Skoglundh, M., Sehested, J., Helveg, S., Ostwald ripening in a Pt/SiO_2 model catalyst studied by *in situ* TEM, *J. Catal.* **281,** 147-155 (2011).

[28] Challa, S. R., Delariva, A. T., Hansen, T. W., Helveg, S., Sehested, J., Hansen, P.L. Garzon, F., Datye, A. K. Relating rates of catalyst sintering to the disappearance of individual nanoparticles during Ostwald Ripening. *J. Am. Chem. Soc.* **133,** 20672–20675 (2011).

[29] Yang, F., Chen M. S., Goodman, D. W. Sintering of Au particles supported on $TiO_2(110)$ during CO oxidation. *J. Phys. Chem. C* **113,** 254-260 (2009).

[30] Zheng, X., Bigot, B., Ostwald ripening on a substrate: modeling local interparticle diffusion. *J. Phys. II France* **4,** 743-750 (1994).